

Chapter 1

The Periodic ‘Flapping’ and ‘Breathing’ of Saturn’s Magnetodisc During Equinox

In this chapter, we present the results of an investigation into the periodic displacement and thickness modulation of the equatorial current sheet at Saturn. Magnetic field observations by *Cassini*’s MAG instrument suggest that in the outer magnetosphere (beyond $\sim 12 R_S$) Saturn’s current sheet is periodically displaced with respect to the rotational equator with a period close to the planetary rotation rate, to a first approximation acting as a rotating, tilted disc. This manifests as a ‘flapping’ mode when observed by *Cassini*. Recent studies suggest the magnetosphere also has a ‘breathing’ mode, expanding and contracting with a period close to the planetary rotation rate, correlating with a modulation in the thickness of the equatorial current sheet. In the study in this chapter, we model these two modes in tandem by combining a global, geometrical model of a tilted and rippled current sheet with the UCL/AGA force-balance model of Saturn’s magnetodisc described in Section 1.5, accounting for the magnetospheric size and hot plasma content. We simulate the breathing behaviour by introducing an azimuthal dependence of the system size. We fit Cassini MAG data acquired on equatorial orbits from 23 Oct-17 Dec 2009 (Revs 120-122), close to Saturn equinox, in order that seasonal effects on the current sheet are minimised. We find that our model characterises well the amplitude and phase of the oscillations in the data, for those passes that show clear periodic signatures in the field. In particular, the B_θ (meridional) component can only be characterised when the breathing mode is included. This study introduces

calculations for an oscillating boundary, which provide a basis for understanding the complex relationship between current sheet dynamics and the periodic field perturbations.

The content of this chapter is based on the study:

1.1 Introduction to this Study

Recent observations of Saturn’s magnetic field suggest that the planetary dipole axis and rotation axis are aligned to $\leq 0.01^\circ$ (?). However despite this extremely high degree of axisymmetry, periodic variations have been observed in field and particle properties throughout Saturn’s magnetosphere, modulated at a period close to the planetary rotation rate. These observations are summarised in ?, and also discussed in Section 1.4.1 of this thesis. Of particular interest to the study in this chapter are the periodic perturbations observed in the magnetic field, and the influence they have on global magnetospheric structure.

Even before the *Cassini* spacecraft arrived at Saturn, analysis of legacy magnetometer data from the *Voyager* and *Pioneer* missions had revealed periodic perturbations in the magnetic field, which could not be adequately explained by a true dipole tilt (?). This led to the development of a ‘camshaft’ model, where a rotating equatorial magnetic anomaly that is fixed in planetary longitude triggers radial waves that propagate through the magnetosphere and cause the observed perturbations (?). It is therefore a key focus in the scientific community, to create a reliable Saturn longitude system to organise these observations. To further complicate this picture, *Cassini* magnetic field observations then revealed two distinct periods in the magnetic field perturbations, associated separately with the Northern and Southern hemispheres (e.g. ??). In these and other studies, such as ?, a picture has now been developed of how these hemispheric magnetic perturbations are generated, by two large-scale field-aligned current systems that rotate at slightly different rates in each hemisphere. The magnetic field associated with each current system is dominant in the respective hemisphere, and can be approximated in the outer magnetosphere by a rotating, transverse oriented dipole. The physical origins of these

current systems are also still not fully understood, but are thought to be associated with twin atmospheric vortices flowing in the polar upper atmosphere/ionosphere in each hemisphere (??). During the initial *Cassini* mission, the southern magnetic perturbation was dominant over the northern, and had a longer period of ~ 10.8 h compared to ~ 10.6 h. However after Saturn equinox in August 2009, the two perturbations slowly converged in terms of both time period and amplitude, before diverging again (?).

In this study we focus on the effect of these dual rotating magnetic perturbations on Saturn's outer magnetosphere. To do this, it is helpful to first consider the picture put forth in ?? and references therein, of the two hemispheric perturbations being approximated by rotating transverse dipoles, each with associated magnetic field only felt in the respective hemisphere. In the magnetosphere's equatorial 'core' region, within radial distances of $\sim 10\text{--}15 R_S$ and thus within the magnetic shells of the associated field-aligned currents (e.g. ?), the resulting magnetic perturbation field is rotating and quasi-uniform in magnitude. On higher-latitude field lines, and beyond the core region, the perturbation field can be approximated in each hemisphere by a dipole magnetic field whose axis lies in the rotational equatorial plane. The influence of these magnetic perturbations on the global magnetodisc structure is shown by the diagram in Figure 4.1, reproduced with permission from ?. The magnetospheric magnetic field, made up of Saturn's planetary dipole field and the magnetodisc field, is shown by the black lines in panels (a) and (c), whilst the perturbation fields associated with the Northern and Southern hemispheres are shown in blue and red respectively. The effect of these perturbation fields on the total magnetospheric magnetic field is then shown by the black lines in panels (b) and (d). The direction in which the effective 'transverse dipole' points can be ascertained via an analysis of the oscillations in the magnetic field data (e.g. ?), defined in each hemisphere by a phase $\Psi_{N,S} = 0^\circ$. The evolutions of $\Psi_{N,S}$ over time can then be used to define a physically meaningful longitude system for the planet, based on the magnetic perturbations. Alternatively, observations of perturbations in the Saturn Kilometric Radiation (see Section 1.4.1) can also be used to create a similarly time- and hemispheric-dependent longitude system (e.g. ?). This longitude system could be used to organise the observed perturbations in other magnetospheric properties

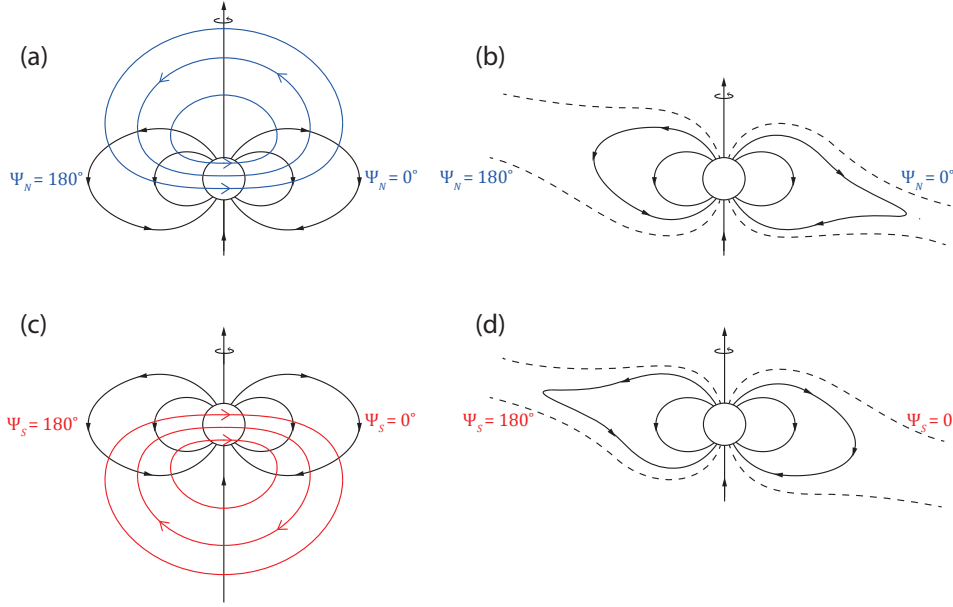


Figure 1.1: Sketches showing the planetary magnetodisc magnetic field in black lines, and the magnetic field associated with the northern and southern hemispheric magnetic perturbations, in blue and red respectively. Panels (b) and (d) show the result of the superposition of the magnetodisc and perturbation magnetic fields shown in (a) and (c). Reproduced with permission from ?.

described in Section 1.4.1.

A key effect of the hemispheric magnetic perturbations on Saturn's magnetodisc is a periodic motion of the equatorial current sheet above and below the rotational equator, or 'flapping' behaviour as perceived by a stationary observer. This is a separate phenomenon to the displacement of the entire current sheet northwards into a bowl-like shape observed by ? during the initial *Cassini* mission, which was due to the incoming direction of the solar wind plasma impacting the magnetopause from the south during Saturn's southern summer. In the transverse dipole approximation, this flapping we describe can be understood as follows. At $\Psi_{N,S} = 0^\circ$, the radial component of the perturbation field adds to the planetary magnetodisc field north of the equator, and subtracts from the background field south of the equator. The opposite is true at $\Psi_{N,S} = 180^\circ$. Magnetic pressure balance must be approximately maintained across the lobes of the current sheet (i.e. regions just outside) and thus this has the net effect of a rotating perturbation, acting to displace the equatorial current sheet southward below the rotational equator at the particular longitude defined by $\Psi_{N,S} = 0^\circ$, and northward at the diametrically opposite longitude, as shown in Figure 4.1 (b), (d). As the whole pattern rotates, this rotating tilted

magnetodisc appears to a stationary observer as a periodic vertical flapping of the current sheet, as it passes above and then below the rotational equator once per rotation period.

This behaviour has been detected, and quantified to some extent, in studies using various *Cassini* datasets. ? analysed signatures of periodic equatorial current sheet crossings observed in the magnetic field data by *Cassini* MAG on equatorial orbits in 2006. They determined that, in the outer magnetosphere beyond $\sim 12\text{--}15 R_{\text{S}}$, the total magnetic field can be approximated by a rotating tilted disc, with a tilt angle of $\sim 12\text{--}15^\circ$ relative to the rotation axis. This is in broad agreement with a study by ?, who fitted a model of a tilted and rippled current sheet to MAG and CAPS/ELS data from orbits from 2006. They found that a value of 12° for the effective current sheet tilt provided a good agreement between their model and the data, and that smaller values could not reproduce the amplitudes of the observed oscillations. In contrast, ? analysed magnetic field data from subsequent higher-latitude *Cassini* orbits and found smaller values for an effective dipole tilt of $\sim 5\text{--}10^\circ$, and that the best fit value depended on the component of the magnetic field vector being analysed.

As pointed out in ?, this kind of analysis does not establish the influence of the relative phases of the southern and northern perturbations on the current sheet flapping. The studies discussed so far are based on *Cassini* observations made when the southern perturbation was dominant in amplitude, and thus the observed current sheet tilt was associated with this perturbation only. However, as previously mentioned, after Saturn equinox the two perturbations became similar in amplitude, and so it is important to consider the effect of both. Figure 4.1 illustrates that a maximum current sheet displacement would be observed when the two perturbations are in phase, such that the meridians defined by $\Psi_N = 0^\circ$ and $\Psi_S = 0^\circ$ spatially coincide, and a minimum displacement arises when these meridians are diametrically opposite, and the perturbations are in antiphase. Indeed ? observed in the magnetic field data that the current sheet oscillation was a maximum when the two perturbations were in phase, and some modelling studies such as ? and ? have also investigated this kind of behaviour. However there is still much to be understood, particularly for intermediate perturbation phase differences, and the effect of the

change of phase with radial distance in the outer magnetosphere. In this chapter we look at these effects in more detail.

The other important effect of these magnetic perturbations is the current sheet ‘breathing’ behaviour, that is, a compressional disturbance in the magnetodisc. While the rotational disturbance that causes the flapping behaviour is mainly associated with the *radial* component of the perturbation magnetic field, the compressional disturbance is mainly associated with the *meridional* component. Again looking at Figure 4.1, we can see that for the northern perturbation, the meridional component subtracts from the planetary magnetodisc field at $\Psi_N = 0^\circ$, and adds at $\Psi_N = 180^\circ$. In contrast for the southern perturbation, the meridional component adds to the planetary magnetodisc field at $\Psi_S = 0^\circ$, and subtracts at $\Psi_S = 180^\circ$. Where the perturbation field enhances the planetary magnetic field, this causes a compression of the magnetic field lines into a more dipolar configuration, associated with a thickening of the equatorial current sheet, observed by a stationary observer as a ‘breathing in’. At the opposite longitude, the reduction in the meridional component of the magnetodisc magnetic field causes an extension of the magnetic field lines into a more disc-like configuration, associated with a thinner and more extended current sheet. Unlike the case of the flapping perturbation, this breathing perturbation occurs at opposite phase longitudes for each hemisphere, and so we would expect to observe a maximum compressional disturbance when the northern and southern perturbations are 180° out of phase.

This behaviour was also observed in ?, who found that the thickness of the current sheet was modulated by a factor of ~ 2 when the magnetic perturbations were in antiphase. More recently, ? looked in detail at the expected magnetic field signatures for intermediate perturbation field phase relationships, as a companion study to ?. These studies found instances of ‘sawtooth’ shaped signatures in the radial component of the magnetic field data during current sheet crossings, and, through a comparison with various modelling results, suggested that this was associated with a periodic thickening and thinning of the magnetospheric current sheet. A further study by ? suggests a complex relationship between current sheet thickness in each hemisphere and intermediate perturbation phase differences. In MHD modelling studies there is also evidence for this periodic breathing behaviour in the middle

magnetosphere (?), and a periodic perturbation in the magnetopause boundary location (?), which may be related. As discussed in the Introduction section 1.4.2, ? also found empirical evidence using *Cassini* MAG and CAPS/ELS data that the magnetopause boundary moves periodically by up to $5 R_S$ in the post-noon local time sector, associated with some rotating magnetic perturbation.

In this study we attempt to draw these various strands together, and investigate both the flapping and breathing behaviour of Saturn's magnetodisc. We use an adapted form of the UCL/AGA model to locally represent Saturn's magnetodisc, and 'anchor' it to a global, geometrical model of the current sheet location adapted from ?, in order to model a magnetodisc that displays both behaviours. We compare our model magnetic field predictions to measurements made by *Cassini*'s magnetometer on three equatorial orbits made shortly after Saturn equinox in August 2009. We fit parameters that describe the tilt of the current sheet, and the longitudes of the maximum rotational (flapping) and compressional (breathing) disturbances, for each *Cassini* pass in order to quantitatively understand how the relative phase of the hemispheric magnetic perturbations affects the magnetodisc structure.

In Section 4.2 we present our combined model construction, and discuss how the tilted, rippled current sheet model from ? simulates the flapping of the current sheet. We also describe our use of the UCL/AGA model, how we choose appropriate model parameters for our data set, and the modifications we make to it in this study. We also explain how we simulate breathing behaviour by varying the UCL/AGA magnetodisc model radius we use as a function of longitude. In Section 4.3 we present the best fit parameters we find for each *Cassini* pass in our data set, and discuss what they indicate regarding the variability of the flapping and breathing behaviour. We conclude with a summary and discussion of potential future work in Section 4.4.

1.2 Method

1.2.1 Data

In this study we analysed *Cassini* magnetometer data acquired on three equatorial orbits from 23 October-17 December 2009 (Revs 120-122), closely following Saturn equinox in August 2009. This interval was chosen in order that the seasonal effect of the current sheet deformation into a 'bowl' shape (e.g. ?) is minimised, and the

current sheet is crossed numerous times. We only analysed data observed beyond $12 R_S$ in cylindrical radial distance relative to the rotation/dipole axis, where we expect this dynamical behaviour of the current sheet to occur. The choice of $12 R_S$ in particular is discussed in detail in the next section. The data set was further restricted to ensure all observations are made within the magnetosphere proper by comparing with the list of magnetopause crossings made by *Cassini* provided in the study by ?, and comparing local MAG and CAPS/ELS observations to signatures described in that study, to determine whether *Cassini* was inside or outside the magnetosphere at a given time. We further excluded data within 6 hours of a magnetopause crossing.

These trajectories are shown by the red-blue path in Figure 4.2, with Saturn shown by the solid circle at the origin. The KSMAG coordinate system used represents a rotation about the y axis of the more standard KSM coordinate system. In KSMAG, the z axis points along Saturn’s rotation/dipole axis, the x axis is oriented such that the $x - z$ plane contains the planet-Sun direction, and the y axis completes the right-handed set. A typical model magnetopause surface from ? is shown by the black dashed line. In this data set the maximum radial distance of *Cassini* from the planet is $\sim 42.4 R_S$, the maximum distance of *Cassini* above/below the rotational equator is $z_{\text{KSMAG}} \approx +0.3 / -1.2 R_S$, and the range in magnetic local time is $\sim 15:45$ to 22:45. Since the spacecraft flies close to the rotational equator throughout this interval, we would expect to see near-symmetric oscillations in the radial component of the magnetic field, if the mean position of the current sheet also lies close to the rotational equator.

1.2.2 Current Sheet Surface Model

To model the changing location of Saturn’s equatorial current sheet over time, we used a structural model first applied to Saturn by ?, simplified to exclude the aforementioned bowl-like deformation associated with solstice conditions. The approach in that study was itself a continuation of analogous studies of Jupiter’s magnetodisc (e.g. ??). The model describes a current sheet effectively tilted from the rotational equator by an angle θ_T beyond a cylindrical radial distance ρ_0 , such that the height

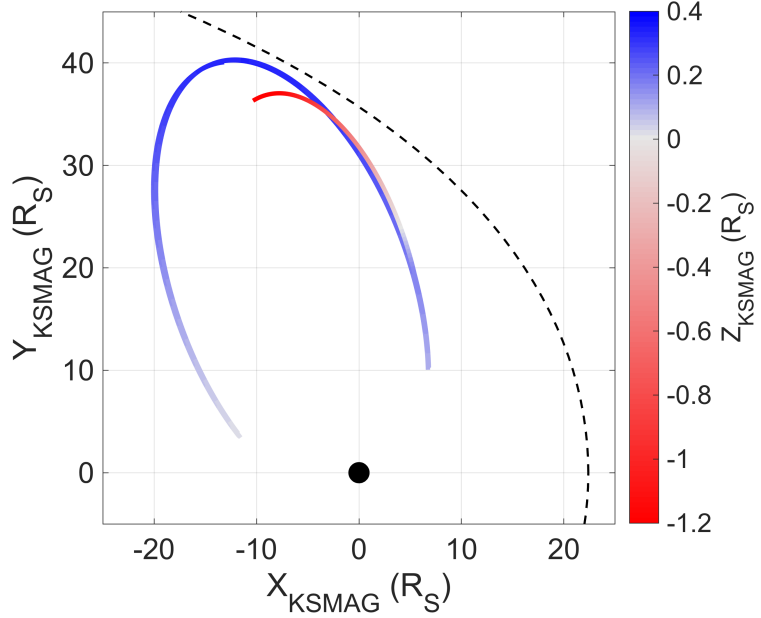


Figure 1.2: The *Cassini* spacecraft trajectory for the period 23 October-17 December 2009 (Revs 120-122), with an anticlockwise orbit. colourbar shows height above and below Saturn's rotational/dipole equator. A typical model magnetopause surface from ? is shown by the black dashed line.

of the current sheet above the rotational equator z_{CS} is described by

$$z_{\text{CS}} = \tan(\theta_T)(\rho - \rho_0) \cos(\lambda - \lambda_0) \quad (1.1)$$

for $\rho > \rho_0$, where ρ_0 is a scale length in cylindrical radial distance which controls the amplitude of the perturbation. We used $\rho_0 = 12 R_S$ in this study, in line with previous results from ? and ?, which suggested that this type of behaviour only becomes significant beyond the magnetic shells of field-aligned currents, as discussed in Section 4.1. λ is an effective phase of this rotating perturbation, related to Saturn longitude λ_{MS} by

$$\lambda = \lambda_{\text{MS}} - (\rho - \rho_0)\Omega_S/v_W, \quad (1.2)$$

such that the tilted current sheet pattern rotates at a rate close to the planetary rotation rate. For λ_{MS} we use the magnetic longitude system of ?, based on *Cassini* MAG observations from 2004 to early 2011. Specifically in this study we use the perturbation signal associated with the southern hemisphere (Ψ_S in Figure 4.1), as this signal was at a similar or greater amplitude than the northern magnetic field perturbation signal for the period studied here (?). We consider the effect of this

choice when interpreting our results later in this study. In particular in Table 4.1 we consider how the observed phase difference between the northern and southern signals from ? influences our results, and at the end of Section 4.3.1 we investigate how our results may be affected by using the magnetic perturbation associated with the northern hemisphere instead of the southern. In addition in Chapter 6, Section 6.2.2 we discuss potential future work in which we could use both northern and southern perturbation information to develop this study further., based on the magnetic field perturbation signal observed specifically in the Southern hemisphere, (Ψ_S in Figure 4.1), as this signal was at a similar or greater amplitude than the northern magnetic field perturbation signal for the period studied here (?). However we do consider the phase difference between the northern and southern signals when interpreting our results, later in this study. λ_0 is an offset parameter which describes the ‘phase front’ of the maximum vertical displacement of the current sheet from the rotational equator relative to λ , which is equivalent to the magnetospheric longitude λ_{MS} at the distance $\rho = \rho_0$. λ_0 is thus effectively a ‘prime meridian’ for this perturbation. The second term in equation (4.2) introduces a radial delay in this perturbation, to account for the time taken for the magnetic perturbation to propagate radially outwards from its source, at an effective wavespeed v_W . This causes a spiral-like pattern in the elevation of the current sheet surface. Ω_S is a variable angular velocity close to the planetary rotation rate of approximately $1.6 \times 10^{-4} \text{ rad s}^{-1}$, corresponding to the angular velocity of the rotating perturbation defined by the λ_{MS} longitude system used here. These two terms can be represented by the single delay parameter

$$D = \Omega_S / v_W, \quad (1.3)$$

where D has units of ${}^\circ/R_S$. The corresponding spiral pattern in the current sheet structure can be seen in Figure 4.3, which shows an example model current sheet surface with typical D , θ_T and ρ_0 parameters as described in the caption. Also shown is a curve of constant phase passing through the maximum z_{CS} at each radial distance, corresponding to $\lambda = \lambda_0$.

In the original study by ? the authors found values of D varying from $2.1\text{--}6.7 {}^\circ/R_S$ from orbit to orbit, with an average of $3.7 {}^\circ/R_S$. This is in broad agreement with the results from ?, who looked for evidence of a spiral pattern in electron

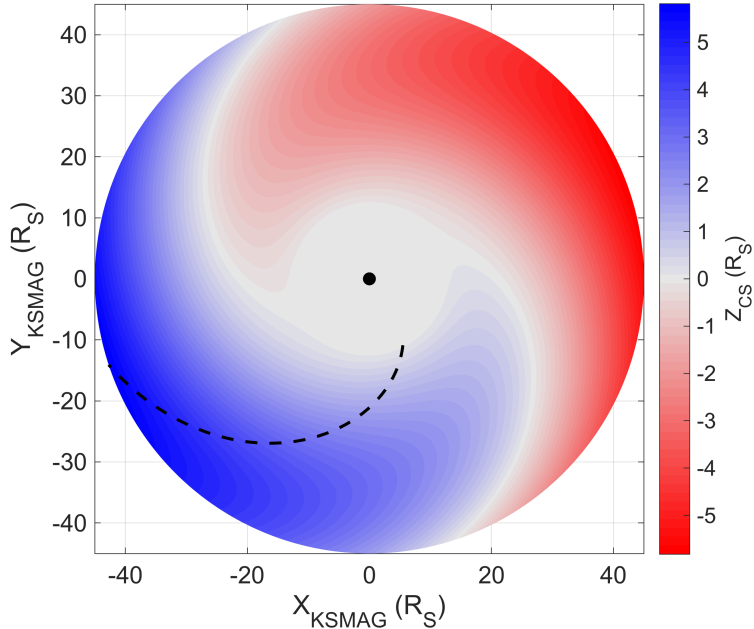


Figure 1.3: An snapshot of the current sheet surface model, with parameters $D = 3^\circ/R_S$, $\theta_T = 10^\circ$, and $\rho_0 = 12 R_S$. Blue and red colour indicates height of the current sheet z_{CS} above and below the rotational equator. The black dashed line represents a curve of constant phase $\lambda = \lambda_0$, passing through the maximum z_{CS} at each radial distance. The whole pattern then rotates with a variable period close to that of planetary rotation.

intensities directly using data from *Cassini*'s MIMI/LEMMS instrument. They observed an average ‘spiral arm migration’ of $\sim 3.4^\circ/R_S$, with a range of $2.7\text{--}4.7^\circ/R_S$. In the study by ?, the authors analyse *Cassini* magnetic field data from a similar time period, to measure how the phase of the magnetic perturbations discussed in the aforementioned ? study varies with radial distance and local time, specifically for the southern perturbation. They find a roughly constant radial phase gradient of $\sim 2.5^\circ/R_S$. On the modelling side, ? used their MHD model of Saturn’s magnetosphere with twin atmospheric vortical flows to stimulate current sheet flapping (as discussed in Section 4.1), and used the modelled current sheet location at different phases and radial distances to estimate a delay of $\sim 4.3^\circ/R_S$. Therefore in line with these studies, we used a value of $D = 3^\circ/R_S$ here, corresponding to a value $v_W \approx 185 \text{ km s}^{-1}$.

In reality, the appropriate parameter $D = \Omega_S/v_W$ would vary with radial distance and local time, as the wave velocity v_W is dependent on plasma parameters and magnetic field strength, which vary throughout the equatorial magnetosphere. Indeed ?, using *Cassini* magnetic field data estimated a radial phase speed that varied

from $\sim 150 \text{ km s}^{-1}$ on Saturn’s nightside to $\sim 500 \text{ km s}^{-1}$ on the dayside, corresponding to D varying from $\sim 3\text{--}1^\circ/R_S$, although they qualify that the dayside value in particular has a high uncertainty. They note that this is at least in broad agreement with estimates based on measurements presented in ? and ?, which suggest typical Alfvén speeds within the equatorial ring current region of $\sim 100\text{--}400 \text{ km s}^{-1}$, depending on magnetospheric parameters. This would correspond to a delay parameter that varies between approximately $D = 6\text{--}1^\circ/R_S$ (where a higher value of D corresponds to a lower value of v_W). We investigated the effect of a variation in D with radial distance of this scale but found it did not significantly influence our results compared to other factors.

1.2.3 Magnetic Field and Plasma Model

The current sheet model geometry described in the previous section must be combined with a local model of magnetic field and plasma sheet structure in order to predict magnetic field values at *Cassini* locations. We geometrically ‘anchored’ a magnetic field and plasma model to our perturbed current sheet surface model following the approach of ?, described in that study and repeated below. For our magnetic field and plasma model, we used a modified version of the UCL/AGA model described in Section 1.5 of this thesis. This model assumes a single mean ion mass along a given magnetic field line, which means that it cannot account for fine structural variation in magnetodisc thickness caused by the concentration of the heavier water ions towards the equatorial plane (e.g. ??). However, as demonstrated in that study, ? and ?, the model can accurately reproduce global average trends observed in Saturn’s magnetodisc. The UCL/AGA model is therefore demonstrably adequate for reproducing the relatively large-scale amplitude oscillations in the magnetic field data that are analysed in this study.

We then extracted magnetic field values from this model along *Cassini* trajectories to directly compare with magnetometer data. The appropriate coordinates ρ_μ and z_μ at which to sample from this model are determined for each *Cassini* observation time by the current sheet model location z_{CS} , according to

$$\begin{aligned}\rho_\mu &= \rho_{\text{S/C}}, \\ z_\mu &= (z_{\text{S/C}} - z_{\text{CS}})\hat{\mathbf{z}} \cdot \hat{\mathbf{n}}\end{aligned}\tag{1.4}$$

where the subscript S/C refers to the *Cassini* spacecraft's actual location, $\hat{\mathbf{z}}$ is the unit vector along the rotation/dipole axis, and $\hat{\mathbf{n}}$ is the unit vector normal to the model current sheet surface calculated according to equation (4.1), using $\rho = \rho_{\text{S/C}}$ and the λ value of the spacecraft location at that time.

The vector components of the magnetic field perturbation (total magnetic field minus the internal dipole) ΔB_i extracted from the model at these coordinates are then transformed back to give the predicted external magnetic field \mathbf{B}_{ext} via

$$\mathbf{B}_{\text{ext}} = \Delta B_\rho \hat{\boldsymbol{\rho}}_{\text{CS}} + \Delta B_z \hat{\mathbf{n}} + \Delta B_\phi \hat{\boldsymbol{\phi}}_{\text{CS}} \quad (1.5)$$

where

$$\begin{aligned} \hat{\boldsymbol{\rho}}_{\text{CS}} &= \frac{\hat{\boldsymbol{\phi}} \times \hat{\mathbf{n}}}{|\hat{\boldsymbol{\phi}} \times \hat{\mathbf{n}}|}, \\ \hat{\boldsymbol{\phi}}_{\text{CS}} &= \hat{\mathbf{n}} \times \hat{\boldsymbol{\rho}}_{\text{CS}} \end{aligned} \quad (1.6)$$

such that $\hat{\boldsymbol{\rho}}_{\text{CS}}$ and $\hat{\boldsymbol{\phi}}_{\text{CS}}$ lie in the local tangent plane of the model current sheet surface, while $\hat{\boldsymbol{\phi}}$ is in the direction of planetary corotation. As the UCL/AGA model is purely poloidal we used $\Delta B_\phi = -\frac{1}{2}\Delta B_\rho$ to characterise the azimuthal magnetic field line bendback, again following ?, adapted from the approach by ?. The internal magnetic field, represented by a dipole situated at Saturn's centre, is then added to this external field to give the total magnetic field at that location.

This formulation effectively assumes that the local magnetodisc structure at *Cassini*'s location may be approximated by the azimuthally symmetric UCL/AGA plasma and magnetic field model, but with the equatorial plane of this model rotated to align with the local tangent plane of the model current sheet surface according to equation (4.1). **This is illustrated by the (not to scale) diagram shown in Figure 4.4.** More details can be found in ?.

1.2.3.1 Model parameterisation

As discussed elsewhere in this thesis, the UCL/AGA model treats the plasma as consisting of a cold population, confined towards the rotational equator due to the centrifugal force exerted on it, and a hot population with associated pressure distributed uniformly along magnetic field lines. In particular we have discussed in

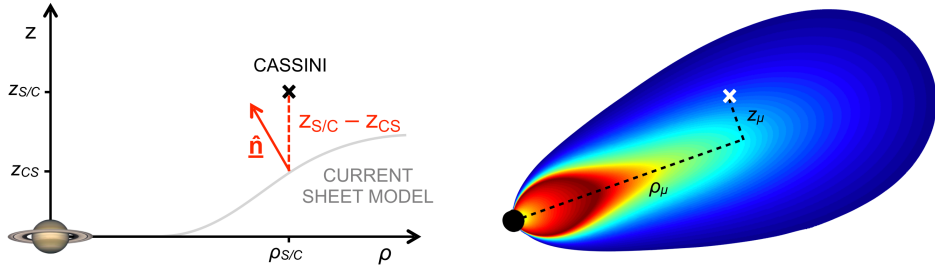


Figure 1.4: Diagram (not to scale) explaining the transformation between *Cassini*'s location in KSMAG coordinates (shown by the black cross) and the coordinates at which the UCL/AGA model is sampled (shown by the white cross). On the left, the model current sheet surface described by equation (4.1) is shown by the grey line, and the vertical distance between this surface and *Cassini* is shown by the red dashed line. The local normal to the model current sheet surface is shown by the red arrow. These values allow calculation of the model sampling coordinates ρ_μ and z_μ as per equation (4.4).

detail the hot plasma index K_H , where $K_H = P_{H0}V$, used to parameterise the pressure of the hot plasma population. In Chapter 3 we explored the effect of varying this parameter within the range 10^5 – 10^7 Pa m T $^{-1}$ on the resulting magnetic field structures. In this study, we used a single value of $K_H = 3 \times 10^6$ Pa m T $^{-1}$, in agreement with the corresponding *in situ* observations made during the period being studied here. This is demonstrated in Figure 4.5, which shows 10-minute-averaged hot pressure moments calculated from *Cassini* MIMI data along the trajectories being studied here, and model predictions of the equatorial hot pressure profile using different K_H values as described in the legend. A third-order polynomial fit of the MIMI data in log-linear space is also shown, in grey, to further illustrate the agreement between the overall trend of the data and the $K_H = 3 \times 10^6$ Pa m T $^{-1}$ model calculations. It should be noted that, as mentioned previously, these *Cassini* trajectories are not exactly equatorial but lie within $+0.3$ / -1.2 R_S of the rotational equator and therefore the comparison between model and data is not exact; however, the variation in pressure associated with transient conditions is much greater than the variation associated with vertical distance from the equator for this data set, and so a comparison with the equatorial model profiles is appropriate here. We consider the potential impact of this assumption on our results in more detail in Section 4.3.

The model can also be parameterised by effective magnetodisc radius R_D , which is the cylindrical radial distance from the origin to the last closed magnetic field line, representing the location of the magnetopause boundary in the equatorial plane. A

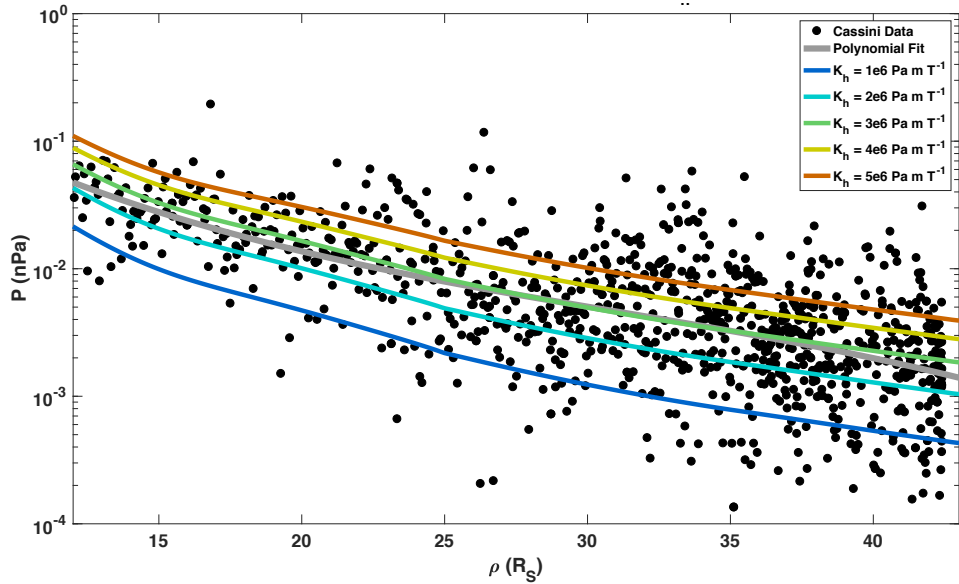


Figure 1.5: Pressure distribution of the hot plasma population in Saturn’s outer magnetosphere, against cylindrical radial distance ρ in the KSMAG coordinate system. Black solid circles show 10 minute averaged hot plasma pressure moments calculated from *Cassini* MIMI data along trajectories Revs 120–122, and coloured lines show equatorial UCL/AGA model profiles using values of K_H as shown in the legend. The grey line shows a third-order polynomial fit of the pressure data in log-linear space, as per the axes.

value of $45 R_S$ was initially used in this study, representing a typical magnetopause boundary location on the dusk flank of the magnetosphere, where *Cassini* spent the majority of its time during the trajectories being studied here, as shown in Figure 4.2. This choice is discussed in more detail in Section 4.2.4.

1.2.3.2 Model modifications for this study

The equatorial profile of plasma angular velocity ω is a boundary condition for the UCL/AGA model, and was updated in this study to better represent the plasma behaviour, particularly in the outer magnetosphere. The original profile was a sixth-order polynomial fit to azimuthal velocity measurements from studies by ?, who used MIMI/INCA data, and ?, who used CAPS/IMS data. We used more recent azimuthal velocity measurements from the study using CAPS data by ?, converted to angular velocities as a fraction of corotation using a planetary rotation rate $\Omega_S = 1.6185 \times 10^{-4} \text{ rad s}^{-1}$ (10.7833 h period). We fit the median values of binned azimuthal velocities in the range $5.5–30 R_S$ with a fourth-order polynomial, to construct an equatorial angular velocity profile. Details of this polynomial are provided in the Appendix A.1, along with a comparison of the original profile from

? For a model with $R_D = 45 R_S$, we found that this profile slightly increased the total equatorial magnetic field strength in the inner and middle magnetosphere, and slightly decreased the equatorial magnetic field strength in the outer magnetosphere, being equal at around $\rho \approx 35 R_S$. The most extreme difference from the original magnetic field strength profile was ~ 1.3 nT at around $\rho \approx 15 R_S$.

In addition, we discussed in Section 1.5 how a small uniform southward-directed ‘shielding field’ is added to the magnetic field perturbation at every iteration, in order to account for the magnetic field associated with the magnetopause and magnetotail current sheets. In the original model construction, the magnitude of this field was chosen by calculating dayside equatorial averages of the empirical field models of ? and ?, and the value varied with model magnetodisc radius R_D (see ?, Figure 6). In particular the component of the shielding field associated with the magnetopause currents was based on a dipole approximation of the magnetospheric magnetic field. However in this study, we calculate magnetodisc models with large R_D such that the global magnetic field structure deviates significantly from a dipolar configuration, and so the magnetic moment associated with the magnetodisc ring current is large compared to the planetary dipole magnetic moment. This can be quantified as the ratio of the ring current magnetic moment to planetary dipole magnetic moment $k_{MD} > 1$. We therefore need to also account for the contribution of the magnetodisc magnetic moment to the magnetopause current. According to ?, the magnitude of this contribution can be approximated to the zeroth order by the field associated with the dipole magnetopause current, multiplied by the ratio k_{MD} , such that the total shielding field component associated with magnetopause currents is enhanced by the factor $(1 + k_{MD})$. Therefore in this study, for ‘large’ models with $R_D > 30 R_S$ we modify the shielding field in this way, using an extrapolation of an empirical fit to *Cassini* MAG data from ? to estimate k_{MD} for each magnetodisc radius. For example, for a model with $R_D = 40 R_S$, we use $k_{MD} \approx 1.3$ and find that this modification enhances the total shielding field in the southward direction by ~ 0.3 nT. We found that a change of this order does not significantly affect the global magnetic field structure, but does improve the tendency for models with more extreme disc radii to achieve convergence.

As a reminder, we consider the UCL/AGA model to have converged when the

relative difference between successive iterations of the magnetic potential solution α falls below a given tolerance, described in Section 1.5. In this study we found that, for models with particularly large disc radii, it was necessary to weight the previous solution up to four times more heavily than the present solution in order to achieve convergence, corresponding to $\gamma = 0.2$ in equation (1.28). This approach, and the modifications to the UCL/AGA model described above, allowed us to calculate models with disc radii as large as $55 R_S$.

1.2.4 Simulating the Breathing behaviour

As described in Section 4.1, Saturn’s magnetospheric current sheet is observed to not only periodically flap above and below the rotational equator, but also to periodically thicken and thin (‘breathing’). In this study we attempted to simulate this compressional perturbation in a novel way, by modulating the magnetodisc radius R_D of the magnetic field and plasma model we sample from, depending on longitude. This is a departure from the study by ?; those authors used a single UCL/AGA magnetodisc model with a fixed value of R_D at all azimuths, and hence did not include the periodic modulation of the current sheet thickness in their model construction. As previously mentioned, the disc radius R_D in the UCL/AGA model is the cylindrical radial distance from the origin to the last closed magnetic field line, representing the location of the magnetopause boundary in the equatorial plane. We use the notation R_D in this chapter to distinguish from the magnetopause boundary location specifically at the subsolar point, R_{MP} , as used in Chapter 3. We showed in the last chapter that in general a model with a larger disc radius has a thinner, more distended current sheet, with magnetic field lines more ‘stretched out’ in the radial direction, due to force balance mainly between the magnetic tension and centrifugal forces. Evidence for this was also shown in the original ? study. In contrast a model with a relatively small disc radius has a more dipolar magnetic field structure, with more compressed field lines, and a correspondingly thicker current sheet.

We used a maximum value for R_D at a phase of the perturbation determined by λ_B , and a minimum value at the opposite phase $\lambda_B + 180^\circ$. We varied this harmonically such that the appropriate R_D to use at any phase λ determined by

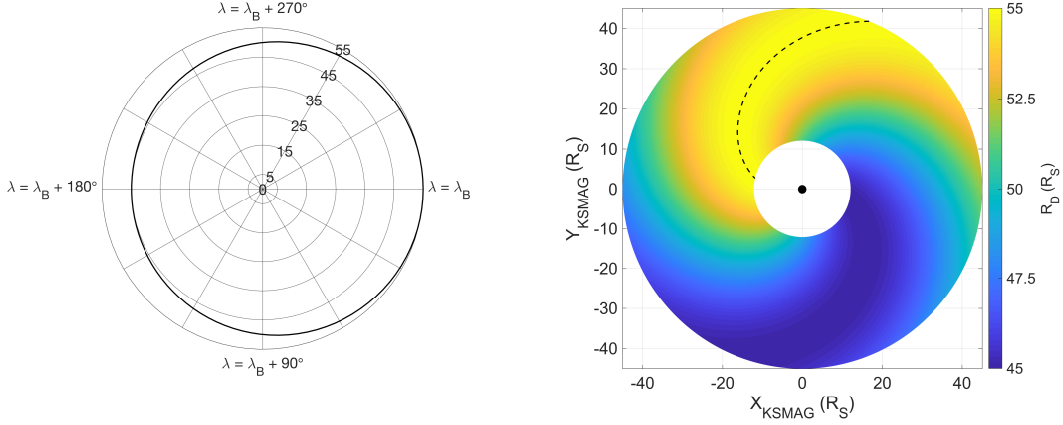


Figure 1.6: (a) How the magnetodisc model radius R_D varies with phase λ , according to equation (4.7). Black solid line shows R_D , grey circles labelled with numbers from 0-55 show radius in units of R_S . (b) Translation of pattern (a) into real space at a given moment in time, according to λ as described by equation (4.2). Colour shows magnetodisc model radius R_D used at each location. The black dashed line highlights where $\lambda = \lambda_B$, and hence a ‘breathing prime meridian’ where the largest disc radius is used.

equation (4.2) is given by

$$R_D = \frac{1}{2} [R_{\text{MAX}} + R_{\text{MIN}} + (R_{\text{MAX}} - R_{\text{MIN}}) \cos(\lambda - \lambda_B)]. \quad (1.7)$$

λ_B is therefore an offset parameter for the breathing perturbation, a ‘prime meridian’ just as λ_0 is for the flapping perturbation. It is used to describe the phase of the maximum equatorial displacement of the magnetopause boundary, and therefore thinnest current sheet, and is measured relative to λ , which is equivalent to λ_{MS} at $\rho = \rho_0$. The entire breathing-related perturbation then follows a spiral pattern with radial distance due to the radial delay in the perturbation propagation, as for the flapping perturbation (see equation 4.2).

This approach is illustrated in Figure 4.6. Panel (a) shows how the model disc radius R_D (shown by the solid black line) varies in λ phase space according to equation (4.7), using values $R_{\text{MIN}} = 45 R_S$ and $R_{\text{MAX}} = 55 R_S$. It can be seen that the largest disc radius is used at $\lambda = \lambda_B$, and the smallest at $\lambda = \lambda_B + 180^\circ$. Panel (b) shows how this then translates into real space for a given moment in time, with colour representing which magnetodisc model radius R_D is used at each location.

To determine appropriate values of R_{MIN} and R_{MAX} , we compared the time period of *Cassini* data being used in this study to the list of *Cassini* magnetopause crossings provided by ?. In particular, we found a period of 5 days (8 - 12 November

2009) where 24 magnetopause crossings were observed in very quick succession, each separated by only a few hours. As discussed in more detail in ?, this suggests that the magnetopause was likely to be close to equilibrium over this time period, as otherwise only a small number of crossings would be observed as the magnetopause boundary moved rapidly over the spacecraft. We assume that the incident solar wind dynamic pressure was roughly constant over this time period, and that the observed perturbation in the magnetopause boundary location was at least in part due to changing internal pressure. This could potentially be associated with the compressional ‘breathing’ magnetic perturbation that we are investigating here, and thus we use this perturbation in the magnetopause location to estimate a reasonable disc radius perturbation.

Figure 4.7 shows the locations of the observed magnetopause crossings in the KSM coordinate system, where x_{KSM} points towards the Sun and $\rho_{Y,Z\text{KSM}} = \sqrt{(y_{\text{KSM}}^2 + z_{\text{KSM}}^2)}$ is the perpendicular distance from this axis. Two potential magnetopause surface locations using the ? model are also shown, both using a value for solar wind dynamic pressure of 0.04 nPa, and with a local plasma β value of 0 for the inner model surface and 1.5 for the outer model surface, to replicate a change in boundary location due to internal pressure changes. These model surfaces were chosen to broadly encapsulate the range of magnetopause crossings in this time period, and thus estimate the corresponding variation in magnetopause radius. However it must be noted that these model surfaces do not represent unique solutions to the crossings shown here and are merely used to get an idea of the changing magnetopause location for this period.

The difference in magnetopause radius of the two magnetopause model surfaces is $21.7 - 18.5 \approx 3 R_S$ at the magnetopause nose. At the dusk flank, along the radial vector pointing from Saturn to the most anti-sunward crossing, this difference increases to $48.3 - 41.1 \approx 7 R_S$. As previously mentioned, a similar and even greater scale of perturbation was observed by ?, who analysed *Cassini* MAG and CAPS/ELS data and found evidence that the magnetopause boundary oscillates by $\sim 1.2 - 5 R_S$ near the magnetopause nose, with a period close to the planetary rotation rate, associated with some internal rotating perturbation. In ? the authors show that an MHD model that accurately predicts the current sheet flapping also produces a

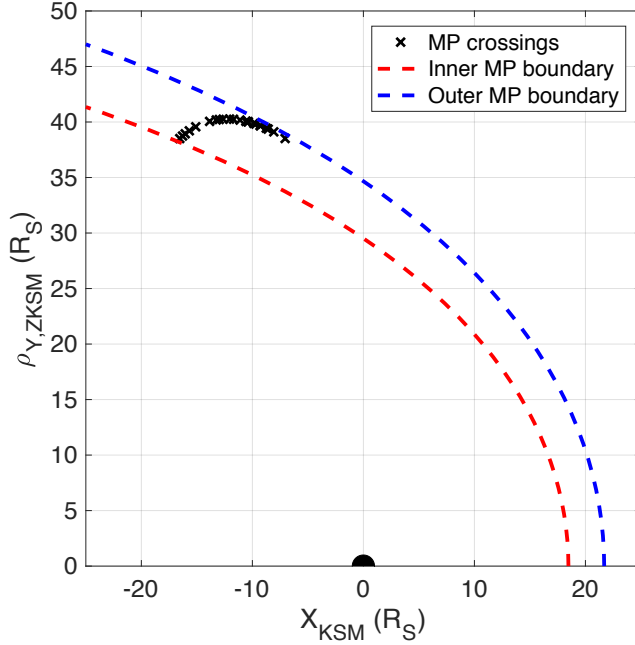


Figure 1.7: Magnetopause crossings observed by *Cassini* in the period 8 -12 November 2009, from ?, in the KSM coordinate system. Model surfaces from the same study are shown in red and blue, using values for solar wind dynamic pressure and local plasma β as described in the main text. Saturn is shown to scale at the origin by the black semicircle.

perturbation of $\sim 5 R_S$ in the nose magnetopause location. In general a given radial perturbation in the magnetopause subsolar location corresponds to a $\sim 2 \times$ greater perturbation at the flank, using a ? style model.

In light of these observations, and our requirement that the minimum model disc radius $R_D \gtrsim 44 R_S$ in order to provide coverage for our entire *Cassini* data set, we used $R_{\text{MIN}} = 45 R_S$ and $R_{\text{MAX}} = 55 R_S$. This perturbation of $10 R_S$ was chosen to simulate the perturbation in the magnetopause boundary particularly on the dusk flank, where *Cassini* spent most of its time for the trajectories being studied here (see Figure 4.2). We calculated a family of five reference models with R_D linearly spaced in this range, and piece-wise linearly interpolated magnetic field values for the required R_D between them, thus assuming that the model magnetic field components at a given ρ, z vary piece-wise linearly with global magnetodisc size R_D . Figure 4.8 (a)-(c) shows plots of how the hot plasma pressure P_H varies in cylindrical coordinates ρ and z for three of the five models we use in this study. As this quantity P_H is constant along magnetic field lines, this effectively shows the magnetic field structure for each of the magnetodisc models. A reference line at $z = 4 R_S$ is included to show that for the larger magnetodisc model with $R_D = 55 R_S$,

the current sheet is thinner and the magnetic field structure is more disc-like than for the models with smaller R_D . Figure 4.8 (d) shows equatorial magnetic field profiles for the five models used in this study. The similarity between the different profiles illustrates that our approach, of linearly interpolating between them to represent outputs from models with intermediate disc radii, is broadly appropriate here. (For comparison, a similar plot but with magnetodisc models calculated with smaller R_D was shown in Chapter 1; Figure 1.6.)

In reality, the thickness of Saturn’s magnetospheric current sheet also varies with local time, with, in general, a thicker and more radially compressed current sheet on the dayside than the nightside (e.g. ?). In order to accurately account for this behaviour, the value of R_D could be also varied as a function of local time, or the family of magnetodisc models could be otherwise modified to more accurately represent different local time sectors. While non-trivial and beyond the scope of this current study, we would like to investigate this in future, and in Chapter 5 we present preliminary results looking at local time variation in current sheet thickness and overall magnetodisc structure. However, for this study, our current approach is appropriate in this context and unlikely to significantly affect our conclusions. This is because we analyse each *Cassini* pass individually, and the range in local time for each pass is only $\sim 2\text{--}3.5$ hours, as shown by the annotations at the bottom of Figures 4.9–4.14. This means that any variation in current sheet thickness associated with local time is likely to be less significant than the variation due to the magnetodisc breathing behaviour.

1.2.5 Fitting Procedure and Parameter Uncertainty Estimation

We fit the model to all three components of the 1-hour averaged magnetic field vector data measured by *Cassini* in spherical polar coordinates, with $\hat{\phi}$ in the direction of planetary corotation, $\hat{\mathbf{r}}$ pointing radially away from the planet, and $\hat{\theta}$ completing the right-handed set. We separated our *Cassini* trajectories into inbound and outbound passes, and fit the current sheet model parameters relevant for each pass. For the ‘flapping only’ model, we use a fixed magnetodisc radius $R_D = 45R_S$ and fit the parameters θ_T and λ_0 , and for the ‘flapping and breathing’ model we use a range of disc radii as described above, and fit θ_T , λ_0 and λ_B . We used a standard non-linear

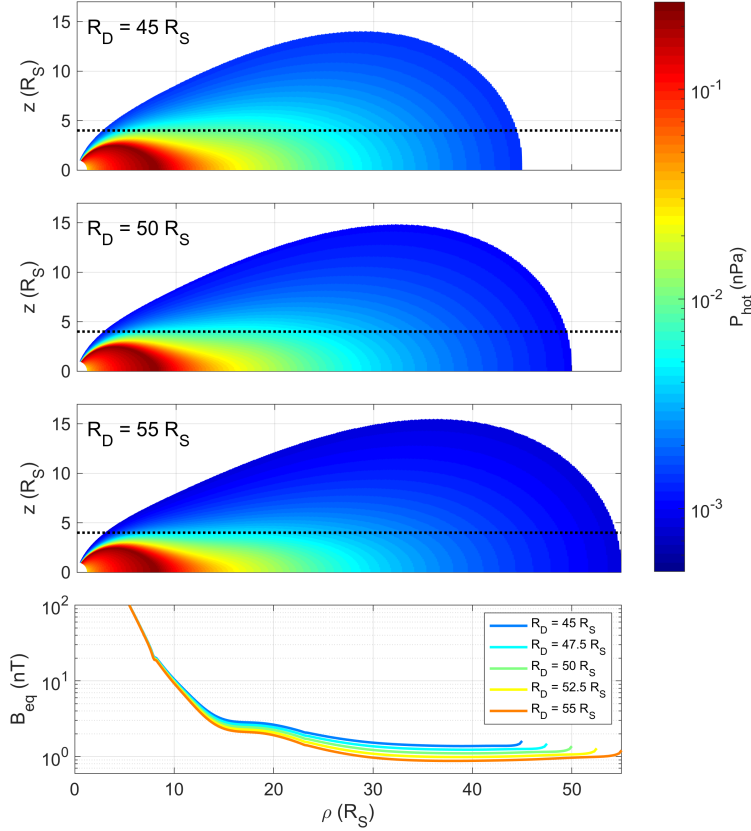


Figure 1.8: (a)-(c) Hot plasma pressure P_H predicted by the magnetodisc models as a function of cylindrical coordinates ρ and z , shown on a colour scale as per the colourbar. Models calculated using model disc radii R_D (a) $45 R_S$, (b) $50 R_S$ and (c) $55 R_S$. The quantity P_H is constant along a given magnetic field line and thus contours are equivalent to magnetic field lines. Black dotted line at $z = 4 R_S$ is superimposed on each plot for reference, to compare current sheet thicknesses for each model. (d) Radial profiles of equatorial magnetic field strength for each of the five models used in this study, as shown by the legend.

least squares fitting method, minimising the unweighted merit function

$$\chi^2 = \sum_{i,k} (B_k - \hat{B}_k)_i^2 \quad i = 1, \dots, N; \quad k = r, \theta, \phi \quad (1.8)$$

effectively the sum of the squared differences between the model and data magnetic field vector components, where B_k is the observed and \hat{B}_k is the model vector component for each of the N data points. We minimised this function using the Levenberg-Marquardt algorithm, and used the square root of the diagonal elements of the resulting covariance matrix to estimate the standard error, and thus 95 percent confidence limits on the fitted parameters, following ?.

Table 1.1: Fitted parameters θ_T , λ_0 and λ_B for each Cassini revolution (Rev) using the flapping only ('FO') model and the flapping and breathing ('F&B') model, with 95% confidence limits. Also shown is the root-mean-square difference (RMS) between model and data magnetic field values, and the approximate phase difference between the Southern and Northern magnetic perturbations at the centre time of each pass from ? (S-N).

Rev	Model	θ_T (°)	λ_0 (°)	λ_B (°)	RMS (nT)	S-N (°)
120 IN	FO	17.0 ± 2.4	247 ± 6	-	1.16	286
	F&B	14.3 ± 1.8	244 ± 6	20 ± 30	1.06	
120 OUT	FO	5.0 ± 1.3	139 ± 14	-	0.82	237
	F&B	3.6 ± 1.0	134 ± 16	310 ± 40	0.81	
121 IN	FO	7.4 ± 1.8	5 ± 13	-	1.19	156
	F&B	6.4 ± 1.4	11 ± 12	270 ± 40	1.12	
121 OUT	FO	10.4 ± 2.0	268 ± 9	-	0.65	99
	F&B	8.4 ± 1.2	259 ± 7	191 ± 22	0.53	
122 IN	FO	14.9 ± 2.5	280 ± 8	-	1.27	52
	F&B	18.4 ± 2.3	285 ± 5	200 ± 30	1.16	
122 OUT	FO	8.1 ± 1.5	205 ± 10	-	0.90	10
	F&B	6.8 ± 1.4	202 ± 11	310 ± 40	0.97	

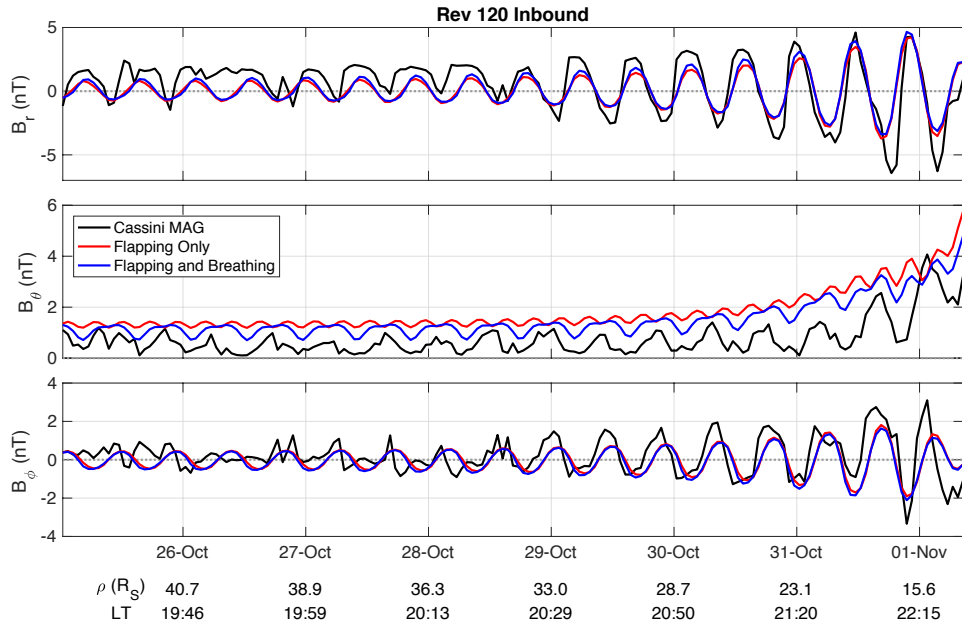


Figure 1.9: Radial (a), meridional (b) and azimuthal (c) components of the magnetic field measured by *Cassini* along **Rev 120 Inbound**, outside of $\rho = 12 R_S$ and inside the magnetosphere. In black we show the MAG data, in red is the flapping only model, and in blue is the flapping and breathing model, both with best fit parameters shown in Table 4.1. Annotation labels underneath give ρ , the cylindrical radial distance of *Cassini* from the planet in KMSAG coordinates, and the Saturn magnetic local time of *Cassini*, LT.

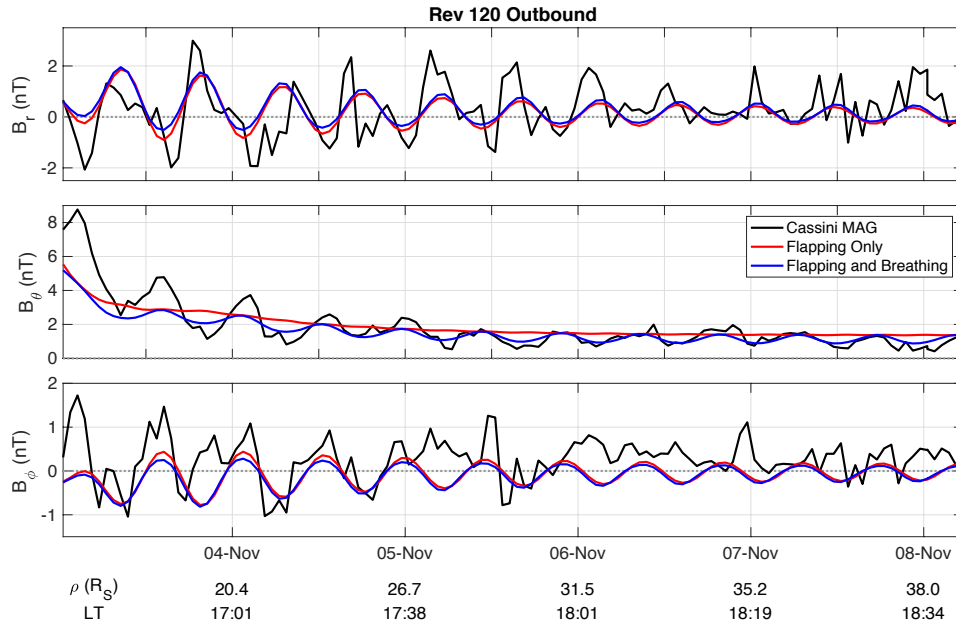


Figure 1.10: As for Figure 4.9 for Rev 120 Outbound.

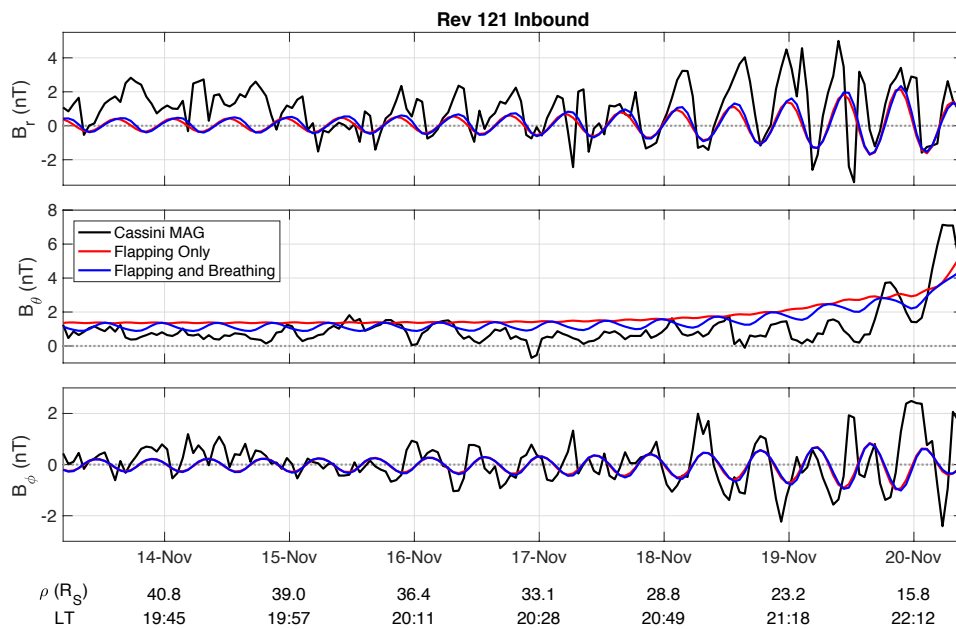
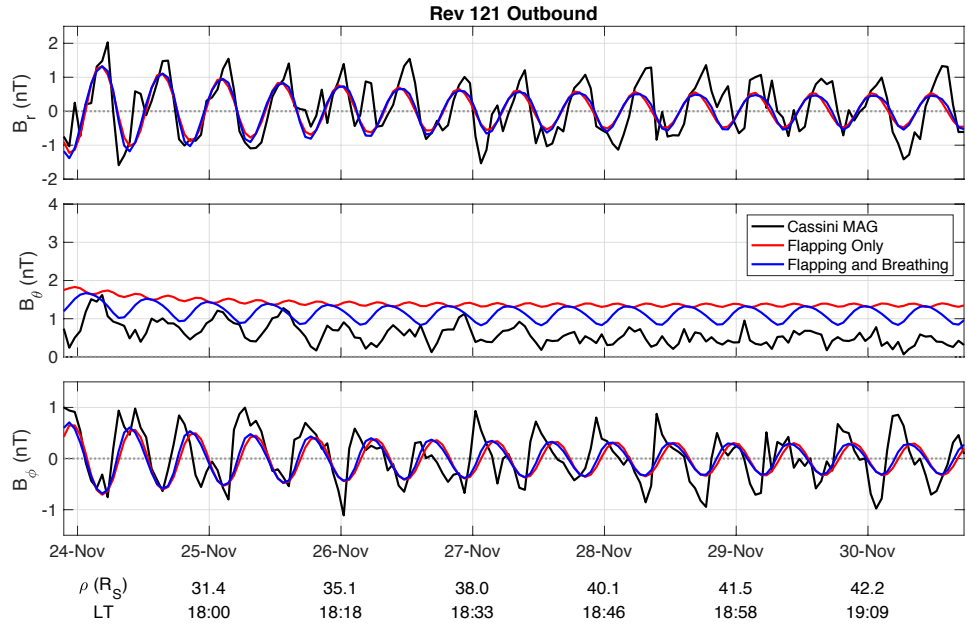
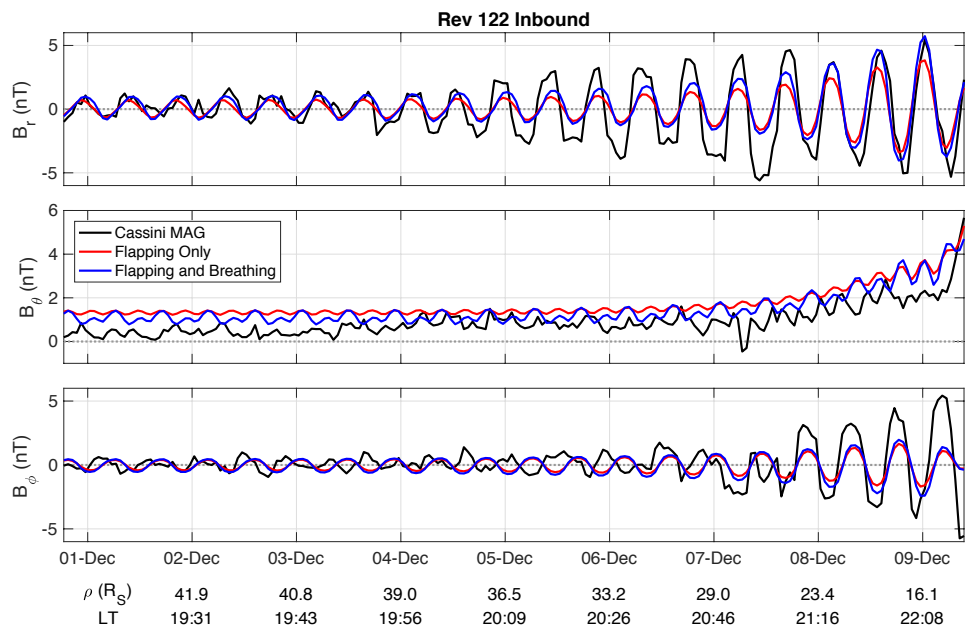


Figure 1.11: As for Figure 4.9 for Rev 121 Inbound.

**Figure 1.12:** As for Figure 4.9 for Rev 121 Outbound.**Figure 1.13:** As for Figure 4.9 for Rev 122 Inbound.

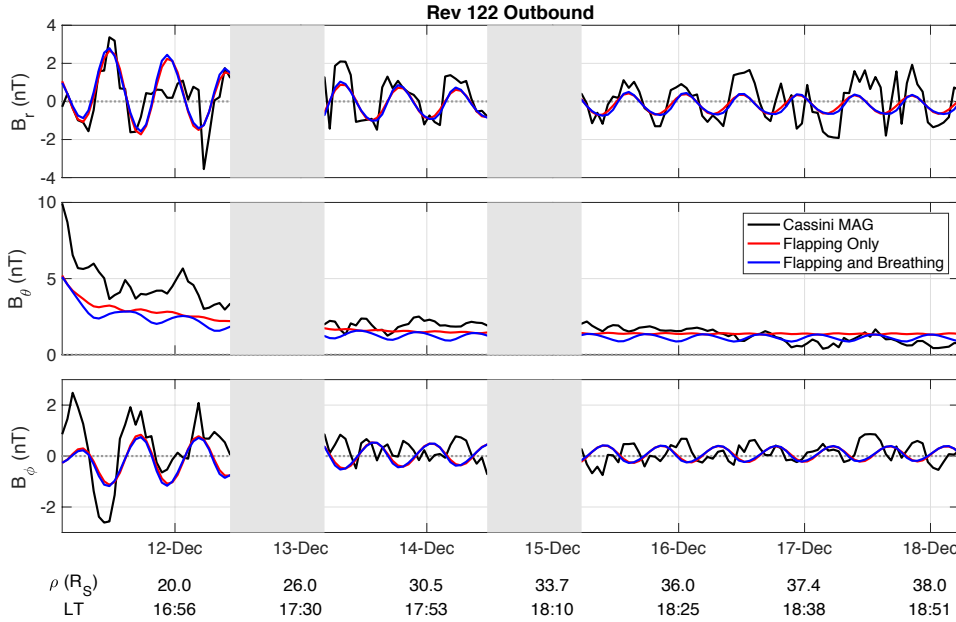


Figure 1.14: As for Figure 4.9 for **Rev 122 Outbound**. The grey shaded regions correspond to where *Cassini* was outside of the magnetosphere and so the model was not fit to data in these regions.

1.3 Results and Discussion

1.3.1 Results with Flapping Only, and With Influence of Breathing

Figures 4.9 to 4.14 show the Cassini magnetic field data acquired on each pass, and the predictions by the ‘flapping only’ and ‘flapping and breathing’ models. The corresponding best fit parameters are shown in Table 4.1. Also shown is the root-mean-square difference (RMS) between the model and data magnetic field values for each model, equivalent to $\sqrt{(\chi^2/n)}$.

In general we can see that for passes that show clear periodicities in the magnetic field data, the ‘flapping only’ (FO) model characterises these oscillations well, particularly in the radial (B_r) and azimuthal (B_ϕ) components. This is most clearly shown in Figures 4.9 and 4.12. For all passes, the best fit values of θ_T with the FO model are in broad agreement with the literature discussed in Section 4.1, although with considerable variation pass to pass. Note that the y-axis scales are not exactly the same for Figures 4.9 to 4.14, and that therefore the amplitudes of the oscillations in the magnetic field data significantly vary from pass to pass. Similarly for λ_0 , with the exception of Rev 121 Inbound, our values are consistent with those of ?, who found their fits for a parameter equivalent to λ_0 varied from $101\text{--}292^\circ$ between passes.

However we can also see that in almost all passes, the FO model does not well reproduce the oscillations in the meridional (B_θ) component. Similar discrepancies between model and data were observed in ?, who used a similar model construction as for the FO model discussed here. (In ? the measured meridional component of the magnetic field was not compared to the model prediction.) In particular in this study, the FO model predicts an oscillation in B_θ of very small amplitude compared to the observations, and with a period approximately twice that of the rotation period. This can be understood as follows: in the FO model, the only source of periodicity is the vertical displacement of the current sheet, which moves across the spacecraft twice per planetary rotation, once from above the rotational equator and once from below. In this picture the B_r and B_ϕ components are both oppositely oriented either side of the current sheet, with B_r maximum positive above the current sheet due to the magnetodisc magnetic field structure, and B_ϕ maximum negative above the current sheet due to the bending back of magnetic field lines, due to the lag in plasma corotation. These components are then reversed when *Cassini* is under the current sheet, and therefore even for the relatively simple FO model, these magnetic field components show a full oscillation roughly once per planetary rotation, in antiphase with each other. In contrast, in the FO picture, B_θ varies symmetrically either side of the current sheet, with a maximum near the current sheet centre and a minimum both above *and* below, and hence it varies twice per planetary rotation, maintaining the same (positive) algebraic sign. For observations where *Cassini*'s orbit is persistently above or below the flapping current sheet, this would appear as a single oscillation in B_θ , once per planetary rotation, with a single maximum observed when the current sheet is closest to the spacecraft. However in the trajectories being studied here, as shown in Figure 4.2, *Cassini* is orbiting extremely close to the rotational equator and thus close to the mean location of the current sheet. Therefore the current sheet flaps fully above and below the spacecraft every rotation, giving a double oscillation in the B_θ component, with only a very weak amplitude.

It is for this reason that the F&B model much better characterises the B_θ component in these instances. This is particularly clear in Figures 4.9, 4.10, 4.11 and 4.12, where the introduction of the breathing behaviour improves the characterisa-

tion of both the amplitude and phase of the oscillations in B_θ . Specifically for the phase, we now observe an oscillation in B_θ only approximately once per planetary rotation. In the ‘breathing’ picture we discussed in Section 4.1, this is interpreted as the ‘breathing in’ or compression of the magnetic field lines and thickening of the current sheet at one phase of the perturbation, corresponding to a maximum in B_θ , and the ‘breathing out’ and thinning of the current sheet at the diametrically opposite phase, corresponding to a minimum in B_θ . As the planet rotates, a stationary observer would pass through each of these phases once per rotation, causing a single dominant oscillation in B_θ , as predicted by the F&B model. The better agreement between this improved model and the MAG data for the passes referenced above supports the picture described in Section 4.1 and illustrated in Figure 4.1, that the rotating magnetic perturbations do cause a periodic modulation in the current sheet thickness as well as location.

For all but Rev 122 Outbound, the F&B model has a slightly lower RMS than the FO model as shown in Table 4.1, suggesting better agreement with the data;¹⁷ however we note that for all trajectories shown here the difference in RMS values between the FO and F&B models is very minor. In addition, the single RMS value for each trajectory does not explicitly reveal how the goodness of fit varies for the different magnetic field components. In Figures 4.9 and 4.12 especially it can be seen that the difference between the FO and F&B model predictions is very small except in the B_θ component, where the F&B model predicts an overall lower magnitude as well as different phase of oscillations. This lower magnitude B_θ for the F&B model is closer to the MAG data for these two passes, and therefore can reduce the overall RMS value even if the phasing of the oscillations does not agree exactly with the data. This is particularly apparent in Figure 4.12 where there appears to be a slight discrepancy in the phasing of the B_θ oscillations between the F&B model and the data particularly at the beginning of the pass, and the F&B model has a lower RMS value of 0.53 nT compared to 0.65 nT for the FO model. In order to try and quantify this more robustly one could investigate the RMS values for each magnetic field component separately; however as the FO and F&B models predict such similar values for the B_r and B_{phi} components, this would likely simply reveal what has just been discussed and can be seen on inspection of the relevant

figures, that the model agreement and RMS value for the B_θ component is sensitive to the overall magnitude of the model predictions as well as the amplitude and phase of oscillations. To investigate the goodness of fit for each magnetic field component in terms of the phasing specifically, the individual components could be fit separately with the FO and F&B models to make independent estimates of the best fit parameters and corresponding uncertainties; however the model parameters would likely not be well constrained when fitting the models to a single component due to the reduced information available. In addition, the FO and F&B models could be fit to different regions of passes rather than entire inbound or outbound trajectories, for example defined by small windows of radial distance. This may reveal how the behaviour of the magnetosphere changes on smaller timescales than individual trajectories and could be useful to investigate in future, along with other potential model improvements as discussed later in this thesis.

The amplitude of the B_θ oscillations in the F&B model is controlled by the harmonic variation in disc radius $R_D = 45\text{--}55 R_S$. In some passes this amplitude appears somewhat underestimated by the model, suggesting a larger range of R_D and thus a larger range in current sheet thicknesses at different longitudes would be more appropriate. However we soon approach the limits of possible convergence for our magnetodisc model when using such high values of R_D , and, as discussed in Section 4.2.4, such large values for the magnetopause location would not be physically justifiable. This issue is a consequence of the model construction, as the variation in current sheet thickness in the model can only be controlled indirectly via the range in R_D . Nevertheless, for illustration, in Figure 4.15 we reproduce the F&B model shown in Figure 4.12 for Rev 121 Outbound, and compare with a model using the same best fit parameters, but employing a larger range of disc radii. In this illustrative model we use the original family of five magnetodisc models as described in Section 4.2.4, supplemented with a larger model with $R_D = 65 R_S$, such that the total range is $20 R_S$. We show this comparison for Rev 121 Outbound in particular because of the approximate 90° difference between the northern and southern perturbation phases, and the best fit values for the flapping and breathing prime meridians, as shown in Table 4.1. This gives good conditions for observing the ‘sawtooth’ signature particularly in the radial component of the magnetic field. As

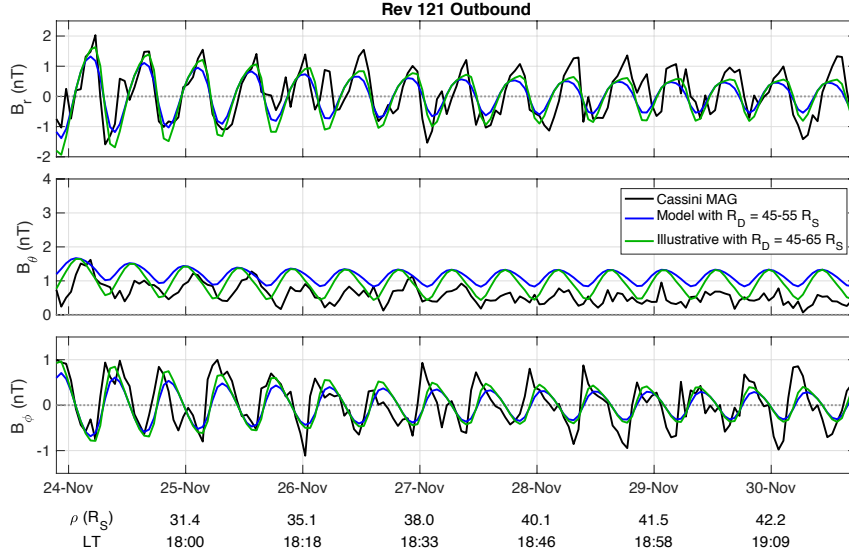


Figure 1.15: Similar to Figure 4.9, for **Rev 121 Outbound**. MAG data is shown in black, in blue is a reproduction of the best fit flapping and breathing model for Rev 121 Outbound from Figure 4.12, and in green is flapping and breathing model using same parameters, but a larger range of magnetodisc model radii as shown by the legend.

described in Section 4.1, this signature is associated with the spacecraft traversing a thinner part of the current sheet in one part of the planetary rotation cycle, and a thicker part in the opposite part (?) and so is more prevalent when there is a more extreme variation in current sheet thickness in different hemispheres. This produces an asymmetric periodic sawtooth-like signature due to the longer time taken to traverse a thicker current sheet.

Reassuringly, when we re-fit this new illustrative model with $20 R_S$ range in R_D to the MAG data for Rev 121 Outbound, we find that the resulting best fit parameters θ_T , λ_0 and λ_B are equivalent to those for our F&B model for that Rev within uncertainties (although note that in Figure 4.15 we show the illustrative model with the exact same parameters as for our original model as shown in Table 4.1, for more direct comparison). However we can see that for the illustrative model the sawtooth signature in the radial field is indeed more pronounced, due to the more extreme range in current sheet thickness for the set of magnetodisc models used here. In addition the amplitude of oscillations in B_θ are greater, for the same reason. This shows the inevitable sensitivity of our results to the chosen magnetodisc model parameters.

The discrepancy between model and data for the average values of B_θ may also

be due to our parameterisation of the hot plasma content K_H in the magnetodisc model. The predicted values of B_θ are sensitive to our choice of K_H , with, in general, higher hot plasma content producing higher magnetic field strengths in the outer magnetosphere, and more disc-like magnetic field structures, due to global force balance, as we saw in Chapter 3, and shown in ?. This type of structure is also, in general, associated with a more extreme variation in the magnitude of the radial component of the magnetic field above and below the equatorial plane. Our choice of K_H could therefore affect our fitting of the tilt angle θ_T , which controls the amplitude of the oscillations in B_r , particularly for the FO model. As discussed in Section 4.2.3.1 we use a value of K_H appropriate for the entire data set studied here, and in line with previous results of global average values. However the appropriate K_H for the region local to *Cassini* may well vary from pass to pass depending on local conditions, and we can see from Figure 4.5 that the hot plasma pressure varies significantly within our interval of study. This explanation would also be consistent with the observation that our models underestimate the average B_θ in some passes and overestimate in others, rather than systematically overestimating or underestimating across all passes. This could also potentially explain why we find a range of best fit θ_T values that, while consistent with previous results, show significant spread from pass to pass. However, we find that the observed hot plasma pressure varies significantly from a given model profile shown in Figure 4.5, even within one single Rev as separated in this study. This comparison implies that even using different values of K_H from pass to pass could not capture the hot plasma variations in their entirety. Similar variability has been observed and discussed in studies such as ? and ?.

Additionally, the magnetodisc model assumption of a single ion mass along each field line, previously mentioned in Section 4.2.3, means that the model does not account for fine variation in magnetodisc structure caused by a concentration of heavier ions near the current sheet, which could lead to a putatively thinner current sheet at large radial distance (?). This effect would generally be associated with an even lower value of B_θ than we predict herein, particularly in the outer magnetosphere. Plasma sheet thickness can also vary unsystematically on time scales as short as a single *Cassini* orbit, potentially due to a combination of internal

and external influences, as shown by ?.

Saturn’s current sheet thickness also varies with local time, which is not directly accounted for by our model, as discussed in Section 4.2.4. The range in local time for each *Cassini* pass studied here is only \sim 2–3.5 hours, and so within a given pass any variation in sheet thickness associated with local time is likely to be less significant than the variation due to the magnetodisc breathing behaviour. For the entire data set studied here, the local time range is approximately 15:45–22:45, with 80% of the data in the range 18:00–21:00, which could introduce variations between passes in how well our model characterises the data; however, observation of Figures 4.9–4.14 does not reveal a significant relationship between model-data discrepancies and the local time range of the given pass.

Looking at each pass individually, the best fit parameters for the F&B model are in general consistent with those of the FO model, suggesting that the FO model is an appropriate approximation at least for modelling the B_r and B_ϕ components of the magnetic field for the period studied here. Specifically, for all but Rev 122 Inbound, the fitted values of λ_0 agree for each model within quoted 95% uncertainties, and the fitted values for θ_T are lower for the F&B model than the FO model. This can be understood as θ_T controls the amplitude of the oscillations in the magnetic field associated with the flapping, and so introduction of the breathing behaviour allows some of this amplitude to be ‘accounted for’ by the breathing perturbation. It is perhaps not surprising that Rev 122 Inbound is the exception to this observed behaviour, as Figure 4.13 shows there is very little observed periodic oscillation in B_θ during this pass, meaning the F&B model is not well constrained. In addition, on this pass a transient negative B_θ signature can be seen around 7 December, which is associated with a region of higher density, lower energy plasma in the CAPS/ELS data. This may be a signature of a small-scale ‘ballooning’ instability of the plasma sheet, resulting in a northward turning of the magnetic field in the centre of a localised plasma ‘bubble’, similar to events observed at Jupiter by ?. This event appears to perhaps be immediately preceded by an episode of current sheet thinning, as revealed by larger amplitude oscillations in the radial component of the field compared to both the model predictions, shown in Figure 4.13. This suggests a very dynamic plasma sheet in this region, and perhaps explains why our models do

not reproduce the data for Rev 122 Inbound in particular. It is interesting to note that immediately after the event B_θ appears to peak when B_r is close to 0, perhaps suggesting a return to flapping-only-like behaviour after this event. Similar transient negative B_θ signatures can be seen in Rev 121 Inbound (Figure 4.11) around 17-18 November, and again are accompanied by more variable, aperiodic magnetic field signatures that cannot be characterised by our models.

In general the best fit values of λ_B show large variation pass to pass, and have larger uncertainties as they are only significantly constrained by the behaviour of the B_θ component. As described in Section 4.2.4, this parameter λ_B determines the longitude at which the maximum disc model radius is used at $\rho = \rho_0$, which in our model is the same as the region with the thinnest, most radially distended current sheet. Looking at Figure 4.1, we can see that for a magnetosphere system dominated by the southern perturbation, we would expect values of λ_B and λ_0 to be similar, as the maximum vertical displacement of the current sheet and the maximum radial distortion of the current sheet are at the same longitude in panel (d). While we do observe this for one pass, there is considerable spread among the other passes. Meanwhile for a system dominated by the northern perturbation, from Figure 4.1 we would expect to observe λ_B and λ_0 approximately 180° apart, as in panel (b) the longitude of the maximum vertical displacement of the current sheet is diametrically opposite to the longitude where the current sheet is most radially distended. However we find that our measured values of λ_B are not, in general, compatible with this picture either. This suggests that the northern and southern magnetic perturbations are of similar amplitude during this time period, which indeed was observed by ?, and thus are both controlling the dynamics of the magnetodisc to varying degrees. ? described how the true behaviour of the magnetodisc is more complicated than this simplified interpretation of diagrams of Figure 4.1, with the current sheet thickness modulated differently in the northern and southern hemispheres depending on the phase difference between the two rotating magnetic perturbations. In this study we only explicitly allow one thickness modulation, at the phase $\lambda = \lambda_B$, and so even our F&B model cannot fully resolve this behaviour. ? observed that the modulation in current sheet thickness is most extreme, by a factor of ~ 2 , when the northern and southern perturbations are in antiphase. In this study we use a fixed current sheet

thickness modulation, fully controlled by our chosen range in disc model radius R_D , and so cannot resolve at what phase differences we observe the greatest variation in current sheet thickness. However this could be addressed in a future study either by allowing the range of R_D to vary as a free parameter, or similar alternative approaches, discussed below in Section 4.3.2 and in Chapter 6.

Another complicating factor for our best fit parameters is our choice of the delay parameter $D = \Omega_S/v_w = 3^\circ/R_S$. This predominantly influences the phasing rather than the amplitude of the model oscillations; for larger values of D , the spiral pattern shown in Figure 4.3 becomes more tightly wound, and so the period of the oscillations generally becomes shorter with increasing radial distance. This particularly affects our fitting of the parameter λ_0 , as this parameter also influences the model phasing by controlling the phase of the maximum flapping perturbation. As previously discussed, the data sets studied here are restricted in local time to the dusk sector, with the majority of observations in the local time sector 18:00-21:00, and no single pass spanning more than 3.5 hours of local time. Therefore the aforementioned variation in magnetospheric wavespeeds reported in ? is unlikely to have a large influence. However the possible variation in wavespeeds with radial distance and local conditions, as discussed in Section 4.2.2, may be a source of discrepancy between our models and results.

As a preliminary investigation, we re-fit the F&B model to the Rev 120 Inbound pass data using a greater value for the delay parameter $D = 5^\circ/R_S$, chosen as roughly the upper limit of an expected appropriate value for D as discussed in Section 4.2.2. We found that the resulting best fit parameters were not significantly altered for this fit, with θ_T and λ_B both equivalent to the values presented in Table 4.1 within quoted uncertainties, and the value of λ_0 differing by around 9%, broadly as expected as this parameter is most strongly affected by the phasing controlled by the specific value of D . We also found that the RMS residual between model and data was around 6% greater for this model than for our original model with $D = 3^\circ/R_S$, suggesting this original lower value of D is appropriate for the best fit in this case.

In addition, with the F&B model we attempt to characterise both the rotational flapping perturbation and the compressional breathing perturbation using a single delay parameter. Intuitively, the delay in the flapping perturbation could be

considered to be controlled by the local Alfvén speed of the magnetospheric plasma, with information traveling from the magnetic poles to the current sheet along magnetic field lines, because this is a rotational perturbation causing a displacement of the current sheet. In contrast the breathing perturbation could be considered to be controlled by the plasma magnetosonic speed, with information traveling radially outwards in the equatorial region towards the outer magnetosphere, perpendicular to magnetic field lines, because this is a compressional perturbation. This means that it may be more appropriate to use different delay parameters for the two different perturbations. This more complicated picture for local phase determination is beyond the scope of this current work, but would be rewarding to investigate in future.

As discussed in Section 4.2, in this study we use a longitude system based on the southern magnetic perturbation from ?, as the amplitude of this perturbation was greater than or similar to the northern perturbation in the equinox period being studied here. In addition, this allowed for a direct comparison with the results of ?. However there is no fundamental physical reason why we could not have used a system based on the northern magnetic perturbation instead. While the amplitude of the oscillations in the magnetic field are unlikely to be affected by such a change, the phasing of the oscillations would be, as the rotation period associated with the northern perturbation is shorter than for the southern. However, as discussed in Section 4.1, this difference became smaller in the period after Saturn equinox, to around 0.1 h for the time period being studied here. A preliminary investigation with the Rev 120 Inbound pass showed that the best fit parameters were not significantly altered when using the northern perturbation to organise the oscillations, with the best fit θ_T equivalent to the value presented in Table 4.1 within the measured uncertainty, and the difference between the parameters λ_0 and λ_B for the F&B model also the same within uncertainties to the results presented here. Note that when using the northern perturbation we would not expect the actual absolute values for λ_0 and λ_B to be equal to those presented here, as they would be measured relative to that new longitude system. Therefore only the difference between the two parameters is comparable, and even this value is somewhat influenced by using the new longitude system due to the aforementioned difference in rotation period for the

northern perturbation. Whilst by no means a comprehensive analysis, this result is reassuring and suggests that our main conclusions would not be significantly altered if we were to use the northern perturbation as a longitude system instead.

1.3.2 Consideration of Equilibrium and Constant Solar Wind Dynamic Pressure

If the compressional breathing perturbation, and consequent movement of the magnetopause boundary, is triggered by an internal source within the magnetosphere, then the appropriate family of UCL/AGA magnetodisc models used to simulate this behaviour should ideally represent an equivalent system under constant solar wind dynamic pressure. However in this study, the magnetodisc models contain no source of internal pressure perturbation, but are calculated assuming magneto-static equilibrium for different disc radii, and, therefore, different upstream solar wind dynamic pressures. This is done to try and reproduce the reconfiguration in magnetic field associated with the breathing dynamics. In Chapter 3 we estimated the incident solar wind dynamic pressure D_P corresponding to a given magnetodisc model by simply summing the magnetic and plasma pressure components just inside the magnetopause boundary at the nose of the magnetodisc, thus assuming pressure balance across the magnetopause at the subsolar point. We use the same approach here for our family of magnetodisc models used to simulate the breathing behaviour. However unlike in Chapter 3, our analysis is not restricted to the subsolar nose of the magnetodisc, where the solar wind is normal to the magnetopause surface, and we therefore must account for the angle ψ between the incident solar wind and the magnetopause surface normal. We discussed in Section 1.4.2 how the full form of pressure balance across the magnetopause surface is given by

$$\frac{B_{\text{MS}}^2}{2\mu_0} + P_{\text{MS}} = [k \cos^2(\psi) + \frac{k_B T_{\text{SW}}}{1.16 m_p u_{\text{SW}}^2} \sin^2(\psi)] D_P \quad (1.24 \text{ revisited})$$

from ?, based on the formulation by ?. The terms on the left represent the magnetospheric magnetic and plasma pressures just inside the magnetopause boundary, and the terms on the right represent the component of solar wind dynamic pressure incident on the magnetopause surface, and a smaller component associated with the solar wind's thermal pressure (see ?). $k = 0.881$ is a factor to account for the

Table 1.2: The disc radii R_D of the 5 different UCL/AGA magnetodisc models used in this study to simulate the breathing behaviour, the total magnetic and plasma pressure at the equator just inside the magnetopause boundary P_{EDGE} for each, and the corresponding estimate of solar wind dynamic pressure D_P using equation (1.24).

R_D (R_S)	P_{EDGE} (nPa)	Approx D_P (nPa)
45	0.0027	0.016
47.5	0.0023	0.014
50	0.0020	0.012
52.5	0.0018	0.011
55	0.0016	0.010

diversion of flow around the magnetosphere obstacle, and T_{SW} and u_{SW} are the temperature and speed of the solar wind. It was shown by ? that the estimated dynamic pressure is insensitive to the choice of T_{SW} and u_{SW} as for any reasonable choice, this term is significantly smaller than the first D_P term for the full range of ψ over which the magnetopause surface model is valid. Nevertheless we use the full form of equation (1.24) here with $k_B T_{\text{SW}} = 100 \text{ eV}$ and $u_{\text{SW}} = 460 \text{ km s}^{-1}$ to represent typical solar wind conditions at Saturn, following ?. At the magnetopause nose $\psi = 0^\circ$ as the magnetopause surface is perpendicular to the incident solar wind, and as you move anti-sunward along the magnetopause surface this value increases, and so the second D_P term becomes comparatively greater. At the dusk flank, at the location of the most anti-sunward magnetopause crossing in our data set, shown in Figure 4.7, the ? surface models shown there have $\psi \approx 67^\circ$. This gives a coefficient of D_P in equation (1.24) of $0.135 + 0.033 \approx 0.17$. If we take our magnetodisc model family to be representative of the magnetosphere in that region, we can then estimate the incident solar wind dynamic pressure D_P by the sum of the internal magnetic and plasma pressures just inside the model magnetopause boundary, divided by this value 0.17, following equation (1.24).

Table 4.2 shows this calculation for the family of five magnetodisc models that were used to simulate the breathing behaviour in this study. We can see that the total pressure at the equator just inside the magnetopause boundary (P_{EDGE}), and the corresponding estimate of D_P , is not constant across all models, but is lowest for the largest magnetodisc model and varies by around 60%. Hence, as we indicated earlier, this family of models does not represent a system under constant solar wind dynamic pressure.

For a more physically realistic model, we would ideally be able to simulate the breathing behaviour of the current sheet without the need to modify the implied external solar wind dynamic pressure. One potential alternative approach, which would satisfy this particular condition, is as follows. A single magnetodisc model could be used at all longitudes, with a given disc radius R_D , as for the flapping only model. The breathing behaviour could then be simulated by varying the cylindrical radial distance ρ_μ at which magnetic field values are extracted from the magnetodisc model (see equation 4.4 and discussion). This could be varied harmonically with longitude broadly as R_D is in our current approach, such that the local magnetodisc structure is effectively displaced inwards or outwards with respect to the spacecraft location, depending on the spacecraft longitude, while the effective solar wind dynamic pressure corresponding to that underlying magnetodisc model remains constant. While beyond the scope of the current study, this approach may provide an interesting comparison to the work presented here in terms of the amplitude and shape of the magnetic field oscillations. The potential drawback of this approach is that it would not reveal explicitly how a periodic thickening and thinning of the current sheet affects the magnetic field oscillation signatures, but more how the global magnetodisc magnetic field structure varies with radial distance. While it satisfies the condition that the incident solar wind pressure is not modulated, it is a somewhat artificial method of introducing the breathing behaviour and is thus a low-order approximation of the true behaviour of the magnetodisc.

Alternatively, a longitude-dependent scaling factor representing sheet thickness could be used to multiply the model coordinate z_μ (see equation 4.4. The longitude dependence could be controlled by a free parameter (much as λ_B is used in this study), but we could also potentially fit for the value of the scale factor; in this way we could investigate by how much the current sheet thickness varies for intermediate phase differences between the Northern and Southern magnetic perturbations, and thus compare results more directly with the observations of (?) and (?).

1.4 Summary and Conclusions of this Chapter

In the study presented in this chapter, we have investigated the periodic dynamical behaviour of Saturn’s equatorial current sheet during the period following Saturn equinox in late 2009, using data from *Cassini’s* magnetometer instrument. We

have attempted to model both the periodic vertical displacement of the current sheet above and below the rotational equator ('flapping' behaviour) and the periodic thickening and thinning of the equatorial current sheet, and corresponding change in magnetic field structure from more dipolar to more disc-like ('breathing' behaviour). Both of these behaviours are thought to be controlled by the dual rotating magnetic perturbations that have been observed in Saturn's northern and southern hemispheres.

To do this modelling we have used a local, force-balance magnetic field and plasma model of Saturn's magnetodisc from ? (the UCL/AGA model), and geometrically anchored it to a global, geometric model of current sheet location from ?. The flapping behaviour was simulated by the periodic displacement of the model current sheet location, and the breathing behaviour was simulated by varying the magnetodisc model disc radius, and thus the magnetic field structure, with azimuth around the planet.

We found that, for those passes that show clear periodic oscillations in the magnetic field, our model characterises well both the amplitude and phase of the oscillations. In particular, the meridional component of the magnetic field was in general better characterised when the breathing behaviour was included, as it can better replicate both the amplitude and the dominant variation once per rotation period, rather than twice as with the flapping only model. These observations therefore support the picture described in Section 4.1 and previously observed by studies discussed therein, that the dual rotating magnetic perturbations in Saturn's magnetosphere cause a periodic modulation in the current sheet thickness, as well as in location above or below the rotational equator. In particular, we find that the ? tilted, rippled current sheet model with a value of delay parameter $D = 3^\circ/R_S$ can accurately characterise the periodic flapping behaviour of the magnetodisc, with observed tilt angles θ_T in the range $4 - 18^\circ$ for the trajectories studied here, in line with previous studies discussed in Section 4.1. We also find values of λ_0 that, when using the Southern magnetic perturbation from ?, are broadly consistent with the results of ?. For the breathing parameter introduced in this study, λ_B , we find significant variation between *Cassini* passes, suggesting that this behaviour varies significantly on this time scale relative to the prime meridian of the flapping

perturbation, likely due to the changing strengths and phase differences between the Northern and Southern magnetic perturbations. However we have shown that by harmonically varying the model disc radius by $10 R_S$, from $45 - 55 R_S$, we can semi-quantitatively reproduce the oscillations in the magnetic field components associated with a periodic perturbation in current sheet thickness, as described in previous studies discussed in Section 4.1. This suggests that the variation in current sheet thickness between these different-sized magnetodisc models, shown in Figure 4.8, is broadly representative of the magnetodisc behaviour for the time interval studied.

For some passes the observed magnetic field is very variable on short time scales, perhaps due to local transient events in Saturn’s plasma sheet, and our model is not capable of capturing this dynamical behaviour. In addition, one main drawback of our model is that it does not explicitly take into account the phase difference between the northern and southern rotating magnetic perturbations, instead using the phase of the southern magnetic perturbation in particular to organise the magnetic field data. This limits the physical insights we can draw from our observations, and it would be insightful to develop this aspect of the model further in a future study. Indeed some potential approaches are discussed in Chapter 6. However, the relative strength of the current approach is that the model can capture the observed behaviour of the magnetic field rather well for much of the time interval studied, with relatively few fitted or fixed parameters.

The treatment of the delay parameter D , discussed in Section 4.2, is another area where it may be beneficial to develop this model further, perhaps using other data sets to further constrain the appropriate choice of D , and in particular how it may vary with radial distance and local time. This may improve the agreement between the model and the data particularly in the phasing of the oscillations. A more realistic representation may also elucidate the mechanisms by which the rotating magnetic perturbations, which are thought to originate from vortices in Saturn’s upper atmosphere and ionosphere, actually control the dynamics much further out in Saturn’s outer magnetosphere.

In this chapter we investigated the structure of the current sheet specifically in the local time region 15:45-22:45, with 80% of the data in the range 18:00-21:00. Therefore we did not explicitly account for any local time variations in the current

sheet thickness in our investigation. However in conducting this study it became apparent that an understanding of how the current sheet and overall magnetodisc structure varies at different local time sectors would be useful in future studies looking at this phenomenon. In Chapter 5, we investigate this local time variation in detail using the UCL/AGA model once again, in combination with recently published observations of the hot plasma population from *Cassini* MIMI data.

List of changes

Replaced: advisers	10
Added: (?)	44
Added: Saturn's magnetopau...	46
Added: A homogeneous solut...	48
Replaced: this	48
Added: solution	48
Replaced: 19	48
Replaced: 0.05	48
Replaced: 0.05	48
Replaced: 0.05	48
Added: In particular, in both...	51
Added: The UCL/AGA mod...	52
Added: Figure 2.9 shows data...	67
Added: Throughout the rest o...	78
Added: (78
Added:)	78
Added: This was demonstrat...	83
Added: As discussed in the I...	103
Replaced: , based on <i>Cassini M</i> ...	106
Added: of approximately...	106
Added: This is illustrated by...	109
Replaced: 19	140
Replaced: 0.05	140
Added: , and in particular ve...	140
Replaced: 0.032	142
Replaced: $0.014 \pm 0.002 \text{ nPa}$	144
Replaced: traces based on	147
Added: in the range $\rho = \dots$	147
Replaced: grey	147
Replaced: field line traces based	147
Replaced: calculated traces usin...	148

Replaced: , however	148
Deleted: the	148
Replaced: traces	148
Deleted: In addition, the some...	148
Replaced: 09:00-15:00	148
Replaced: traces	148
Deleted: light	150